How do interfacial shear and gravity affect the oil film characteristics near an aero-engine bearing?

Dr Avick Sinha
Gas Turbine and Transmissions Research Centre
The University of Nottingham, UK
Nottingham NG7 2TU, UK
Avick.Sinha@nottingham.ac.uk

Benjamin Brewster
Gas Turbine and Transmissions Research Centre
The University of Nottingham
Nottingham NG7 2TU, UK
bpb.brewster@gmail.com

Prof Kathy Johnson*
Gas Turbine and Transmissions Research Centre
The University of Nottingham
Nottingham NG7 2TU, UK
Kathy.Johnson@nottingham.ac.uk

Mike Walsh
Gas Turbine and Transmissions Research Centre
The University of Nottingham
Nottingham NG7 2TU, UK
Mike.Walsh1@nottingham.ac.uk

Dr David Hann
Gas Turbine and Transmissions Research Centre
The University of Nottingham
Nottingham NG7 2TU, UK
David.Hann@nottingham.ac.uk

ABSTRACT

Recent demand for reducing carbon emission and for increasing engine efficiency has led aero-engine manufacturers to strive for a better oil flow system. Aero-engine bearing chambers that house the shaft-support bearings are among the most challenging parts of the engine systems and it is imperative to have a proper understanding of the oil flow characteristics inside a bearing chamber to increase the engine efficiency. The present work is focused on experimentally investigating the oil film characteristics near a ball bearing static slot in the co- and counter- current regions at various rotational Reynolds number (Re_ω), loads and liquid flow rates. The experimental investiga-

*Address all correspondence to this author.

tion has been carried out over a wide range of engine relevant Re_ω up to 1.7×10^6 using high-speed imaging and a long distance microscope.

The results show that formation of the oil film on the static elements of the bearing is governed by both gravity and interfacial forces at low Re_ω but only governed by interfacial forces at high Re_ω. The non-dimensional film thickness ranged from 0.71 to 0.18 and decreases with increasing Re_ω. A regime map was obtained based on the waviness of the film interface showing three different types of wave. At all conditions investigated all waves were capillary waves. Re_ω, oil flow rate and gravity were found to have a significant effect on the film thickness (δ) with transitions matching the wave regime map.

NOMENCLATURE

Symbol	Description	Unit
D_h	Hydraulic diameter, $D_h = \frac{2X(r_c - r_s)}{X + r_c - r_s}$	m
F	Frequency of waves	Hz
g	Gravity	m/s^2
L	Load	kN
P	Angular position of the bearing chamber	-
Q	Flow rate	m^3/s
r_c	Outer radius of the static part of the bearing slot	m
r_s	shaft radius	m
V	Bulk velocity of the film	m/s
X	Axial length of bearing slot	m
Γ	Flow-rate per unit length	m^2/s
δ	Film thickness	m
λ	Wave-length	m
ν	Kinematic viscosity	m^2/s
ρ	Density of the oil	kg/m^3
σ	Surface tension of the oil	N/m
τ	Interfacial shear stress	Pa
ω	Rotational speed	rpm
Re_{Liq}	Liquid Reynolds number, $Re_{Liq} = \frac{\Gamma}{\nu}$	-

Re_ω	Rotational Reynolds number, $Re_\omega = \frac{\omega r_c^2}{\nu}$	-

Subscript	Description
L/H	Low or high load

INTRODUCTION

In recent years, there has been a substantial demand for lighter, more efficient and compact aero-engines. This will help the airlines in reducing specific fuel consumption, emissions and noise, thereby taking a step forward towards achieving the targets set by the Advisory Council for Aeronautics Research in Europe Flight-path 2050 and the Clean Sky 2 targets of producing more environmentally friendly aircraft and decreasing the carbon footprint of the aviation industry. The efficiency of an aero-engine gas turbines can be increased by increasing the inlet turbine temperature and also by increasing the overall pressure ratio [1]. Unfortunately, these processes will increase the temperature of the system and the excess heat could also lead to oil fire or coking inside a bearing chamber [2]. It is therefore imperative to have a proper understanding of the oil flow system, so that it can carry away the maximum heat from the engine system, otherwise, excess heat will reduce engine efficiency and is therefore damaging to the environment.

This paper reports research investigating oil flow in a test rig representative of an aeroengine bearing chamber. In the present study experiments into oil film characteristics were carried out at various rotational Reynolds numbers ($Re_\omega = \frac{\omega r_c^2}{\nu}$) with shaft speeds representative of those of commercial aircraft. Here, ω is the rotational shaft speed, r_c is the outer radius of the bearing chamber and ν is the kinematic viscosity of the inlet oil. The inlet oil viscosity is used in this calculation because changes in the oil viscosity will influence the film thickness, droplet shedding and wave characteristics in the domain of interest, which, for this study, is close to the bearings. Limited literature is available on the film characteristics near bearing slots as most of the studies have looked into the bearing chamber whereas in the present study, investigations were carried out close to the bearing. This is the first time experimental investigations on the film characteristics have been carried out for higher shaft speeds ($Re_\omega \geq 1 \times 10^6$). The results from the present study will support an improved understanding of the oil flow characteristics inside a bearing chamber, thereby contributing to the knowledge required for better design and modelling capability. Furthermore, the data presented here may be useful for the validation of CFD models.

Background

An aero-engine bearing chamber houses the bearings that support the shaft and transmit the loads. The oil flow in a bearing chamber is strongly influenced by the interface between the secondary air system and the oil film flows. Typically, oil is supplied to elements within a bearing chamber for lubrication and cooling via directed jets or through under-race feed. The forces on the oil film at the chamber wall represent the tangential momentum due to the rotation of the bearing, gravity, and the interfacial shear due to the air. The design intent is that the oil films carry away most of the heat from the chamber wall [3]. After its journey through the chamber, the hot oil exits from the bearing chamber through the scavenge ports. To prevent any oil exit from a bearing chamber other than via scavenge/vent ports it is sealed, typically by air-blown labyrinth seals. The oil/air mixture undergoes separation and oil is re-circulated through the system via a feed-pump back into the bearing chamber throughout engine operation.

A bearing chamber undergoes considerable thermal and mechanical stress due to the presence of high temperatures coupled with a high speed of rotation. The rotating environment inside the bearing chamber causes the air to mix with the oil, resulting in a complex two-phase flow. Ineffective heat and flow management in the bearing chamber oil flow system can lead to oil coking, fire [2], and oil degradation [4]. This makes the design and optimisation of the bearing chamber a very challenging task and in many cases more oil is supplied for cooling and lubrication purposes than the minimum required for safety. Consequently, this will increase the weight of the aero-engines. Peduto et al. [5] concluded that higher specific fuel consumption resulting from the additional weight of the oil is due to the lack of understanding of the heat transfer and flow phenomenon inside the oil system. Further investigation of the flow behaviour in a bearing chamber is necessary for a better understanding of the oil-flow system and improved design capability. A key element of oil management in a bearing chamber is film behaviour near the bearing. This is a complex field, measurements are difficult and modelling challenging. Significant progress has been made as outlined in the next section but further research is necessary.

Literature review

In the last three decades, progress has been made on the characterization of oil behaviour in a variety of test modules representative of a number of engine geometries. Experiments have been conducted at various shaft rotational speeds and inlet flow rates to determine flow and heat transfer characteristics for the bearing chambers. At the Karlsruhe Institute of Technology (KIT), Wittig et al. [6] investigated two-phase flow in a simplified chamber containing a roller bearing for two shaft speeds - 7000 rpm and 12000 rpm.

They employed an ultrasonic measurement technique and found that the film thickness on the chamber walls decreases and becomes more homogeneous with the increase in shaft speed due to the increase in shear. Glahn and Wittig [7] used Laser Doppler Velocimetry (LDV) to determine the film velocity profile. They observed that the flow is turbulent for the range of shaft speeds (3000 rpm to 16000 rpm) investigated. This is due to the interfacial shear force between the rotating air and the oil film, which acts as a rough wall. They further observed that increasing the rotational speed increases the shear force, which in turn increases the film velocity and decreases the film thickness.

Guoding et al. [8] analytically investigated the effect of bearing chamber inner housing radii on oil film thickness and velocity to better understanding the influence of impacting droplets. They concluded that with increasing the housing diameter, the average velocity of the film decreases, while the oil film thickness increases. This is because increasing the housing diameter reduces the impacting velocity of the oil droplets and consequently the momentum transferred by the droplets to the oil film. This causes a decrease in the average velocity of the oil film, resulting in the accumulation of the oil film, hence an increase in the film thickness magnitude. Gorse et al. [9], using capacitance probes, observed the effect of shaft speed on the circumferential distribution of oil film thickness. They observed that as the shaft speed was increased, the film thickness distribution along the circumference becomes more uniform. Increasing shaft speed will increase the shear force on the film accelerating and thinning it.

Following on from Gorse et al. [9], Kurz et al. [10] carried out film thickness measurements around the circumference of one of the KIT chambers using a capacitance probe, to investigate the effect of pressure in the bearing chamber. They concluded that as the pressure increases, in the counter-current region (gravity and shear acting in the opposite direction), the film thickness distribution also increases. This is attributed to the change in the properties of the airflow at higher pressure. In Ju et al. [11], it is shown that in pipe flow the interfacial shear is a function of the Weber number which depends on the gas speed, gas density and surface tension. This agrees with Kurz's conclusion.

Various experimental investigations into an aero-engine bearing chamber have been carried out at the Gas Turbine and Transmissions Research centre (G2TRC) at the University of Nottingham for more than 20 years. Chandra et al. [12] conducted experiments on a bearing chamber scavenge using a confocal laser scanning displacement meter to measure the film thickness in the co-current region (gravity and shear acting in the same direction). They observed that at low shaft speed ($\leq$ 5000 rpm) the film thickness decreases as the flow travels down the chamber wall. This is because the flow is accelerating due to gravity as it moves down. However, at higher shaft speed, the film thickness does not vary significantly as it travels.

This shows that shear and centrifugal forces from the rotating flow gas and liquid become more dominant.

The investigations mentioned above focus on the bearing chamber core air flow and films on the bearing chamber walls. More recently, Hee et al. [13] investigated film thickness at various shaft speeds, loads and flow rates on static surfaces very close to the bearing itself. They used an image analysis approach to calculate the mean thickness at various axial planes in the bearing slot for various speeds. A schematic diagram of a simplified bearing chamber is shown in Fig. 1. The prior studies focused on film on the outer stationary wall whereas Hee et al. focused closer to the bearing in the regions labelled on Fig. 1. The bearing slot is the region shown in Fig. 2c. Hee et al. observed that an increase in shaft speed leads to the film at the measuring planes becoming thinner. The film was found to be thinner in the co-current region as compared to the counter-current region (these regions are labelled in Fig. 1) due to the combined effect of gravity and shear, which accelerates the film differently at different locations. Gravity and interfacial shear act in the same direction in the co-current region (90° from top dead centre), while these forces act in the opposite direction in the co-current region (270° from top dead centre). These forces affect the film characteristics and behaviour differently based on Re_ω. Since heat transfer processes are dependent on these characteristics, different heat transfer is inferred based on Re_ω. To date, very little attention has been paid to the effect of gravity and interfacial shear on the characteristics of the film on static surfaces close to the bearing at higher shaft speeds ($Re_\omega > 1 \times 10^6$). These rotational Reynolds numbers are more representative of those experienced by the bearing under operational conditions. Thus, it is imperative to have a better understanding of these forces as obtained in the present study through the measurement of film characteristics at various Re_ω.

The present work was conducted using G2TRC's bearing shedding rig to enhance and complement the prior work carried out using this rig [3, 13, 14]. The research investigates film characteristics at engine relevant Re_ω (up to 1.7×10^6) and for two engine relevant loads and flow rates. Moreover, in this paper, regime maps of film surface characteristics as they change with Re_ω and location are developed based on qualitative observation of the film interface. This work provides a better understanding of the flow phenomenon at the co- and counter-current sides of the bearing.

EXPERIMENTAL SET-UP AND TECHNIQUE

The bearing oil shedding test rig is one of several rigs installed at the University of Nottingham's Gas Turbine Transmissions Research Centre and was used in the present study to investigate the liquid flow behaviour in the co- and counter-current regions close to the bearing. A CAD image illustrating the rig

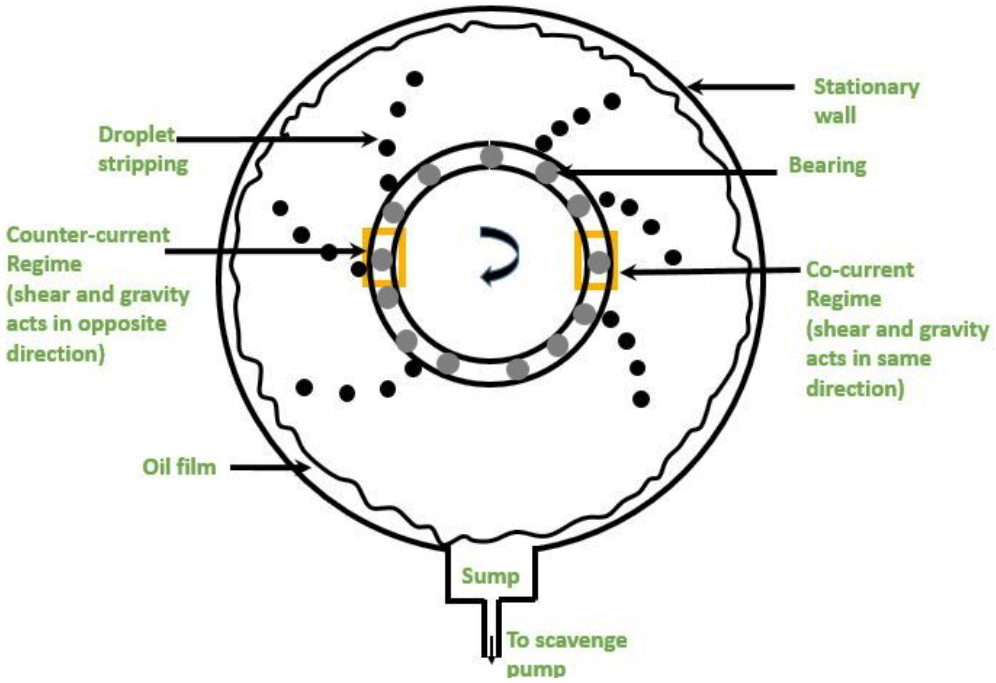

Fig. 1: Schematic diagram of the bearing chamber representing the co- and the counter region.

(from Hee et al. [13]) is shown in Fig. 2a. Gorse et al. [9] observed that the behaviour of the oil shedding depends on the differential pressure across their bearing in the axial direction. To minimise this effect, the bearing shedding rig was designed such that both sides of the bearing chamber are vented to atmosphere. The intent was to minimize the pressure difference across the bearing and also to maintain the pressure inside the chambers close to the ambient condition. The rig front chamber has a transparent window to provide optical access necessary for the imaging. The angular position chosen as 0° is at top dead centre. Investigations in the present study were carried out only on the co-current side (P2, 90°) and the counter-current side (P4, 270°) as shown in Fig. 2b. The film thickness in the present study was measured 3 mm into the slot (between the bearing and the front chamber) as measured from the front face. The location of the measurement plane is exhibited in Fig.2c. This was done by focusing the camera on the front face and then moving it by 3 mm using an analog micrometer.

Two different liquid Reynolds number ($Re_{Liq.} = \Gamma/\nu$= 9 and 13) were chosen in the present study to investigate the effect of the oil flow rate on the film characteristics. Here, Γ is the volumetric liquid flow rate per unit length. The higher of these liquid Reynolds numbers is fully representative for the bearing being investigated. Re_{Liq} is the ratio of the flow-rate per unit length to the viscosity of the oil. The oil used in the present study was Aeroshell Turbine Oil 390 and was fed into the chamber at a temperature

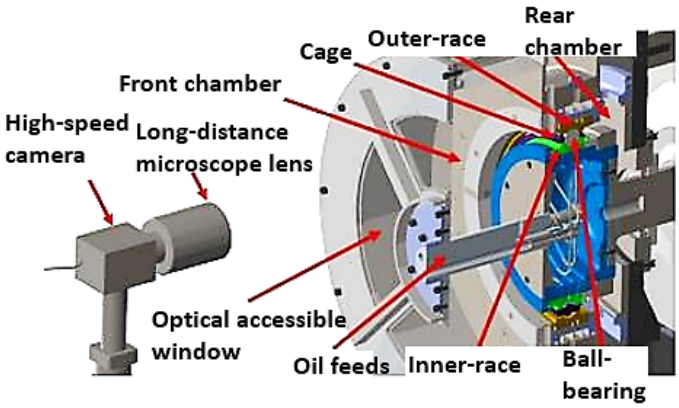

(a)

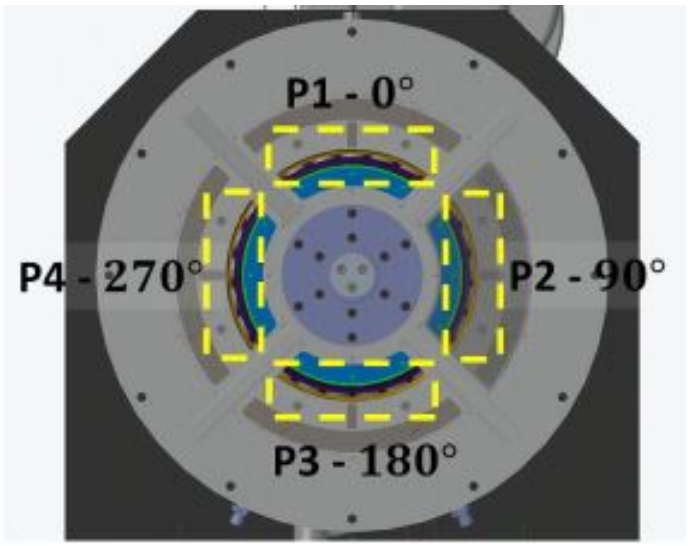

(b)

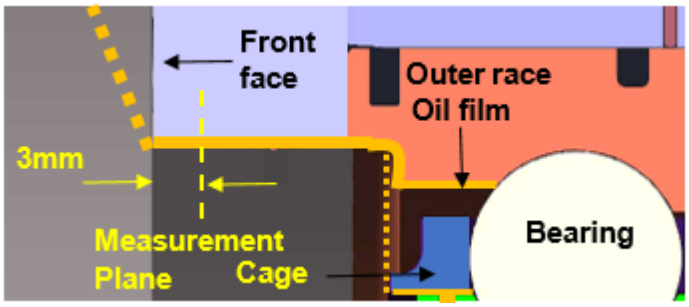

(c)

Fig. 2: (a) Identification of important features in the bearing shedding test rig (b) Naming convention for the different angular positions. P2 and P4 represent the co-current and counter current regions respectively. Images taken from Hee et al. [13] (c) Schematic diagram showing the location of the measurement plane.

of 308K controlled to be within ± 1K. Although the rig operates at temperatures lower than fully engine representative, the chosen oil has lower viscosity so viscosity values are not unrepresentative. The oil is removed from the bearing chambers at the front and rear of the rig using two pumps. It should be noted that Reynolds numbers were calculated using the viscosity of the supply oil and not the local viscosity in the film based on the local temperature. Oil exit temperatures were monitored and it is known that the heat generated in a bearing varies with load, oil supply rate and shaft speed. However, the focus of this work was to attempt to correlate against the inlet condition, which is set and controlled.

In the present study, two different axial loads were considered and applied on the bearing to produce the bearing contact angles which are typically observed in an aero-engine. The two different axial loads in this study are represented as L_L (low load) and L_H (high load), where L_H is three times L_L. An electromagnetic actuator was used to provide the necessary load on the bearing with an accuracy of $\pm$ 2$\%$. The actuators shift the bearing contact angle by pulling the shaft towards the drive and away from the front face. A 49 kW direct-drive motor was used to power the rig to attain a range of Re_ω up to 1.7×10^6. In the present study, 12 different Re_ω were considered from 0.14×10^6 to 1.7×10^6. However, Re_ω from 0.14×10^6 to 0.43×10^6 were only qualitatively investigated as they are of scientific interest but outside normal bearing steady state operation. From the above, it can be concluded that a total of 96 experiments were conducted in the present study based on 12 different Re_ω, two flow rates, two axial loads, and two flow imaging locations (P2 and P4).

Imaging Technique

A high-speed imaging technique was used to obtain the data that are analysed to yield the film statistics. This non-invasive technique eliminates the known calibration errors associated with bubble entrainment in the liquid present with capacitance and ultrasonic measuring techniques [13]. A high-speed camera (IDT vision Os4v3) was attached to a Questar (QM-100) long-distance microscope. The advantage of using a long-distance microscope is that it can have a better resolution of images as compared to a normal camera lens and also have a longer depth of field, thus making it much more sensitive to the change in the film statistics. This will also aid in observing and analysing the dynamics at the liquid-gas interface more precisely. Through calibration, the spatial sensitivity of the long-distance microscope was found to be between 10.3 $\mu m/pixel$ to 11.4 $\mu m/pixel$ for the various cases studied. The images were captured at a resolution of 1024 x 1024 pixels in the vertical and horizontal direction, respectively, with a maximum frequency needed to capture the flow being 4000 Hz supporting image capture over a 1 second period.

IMAGE PROCESSING TO OBTAIN FILM STATISTICS

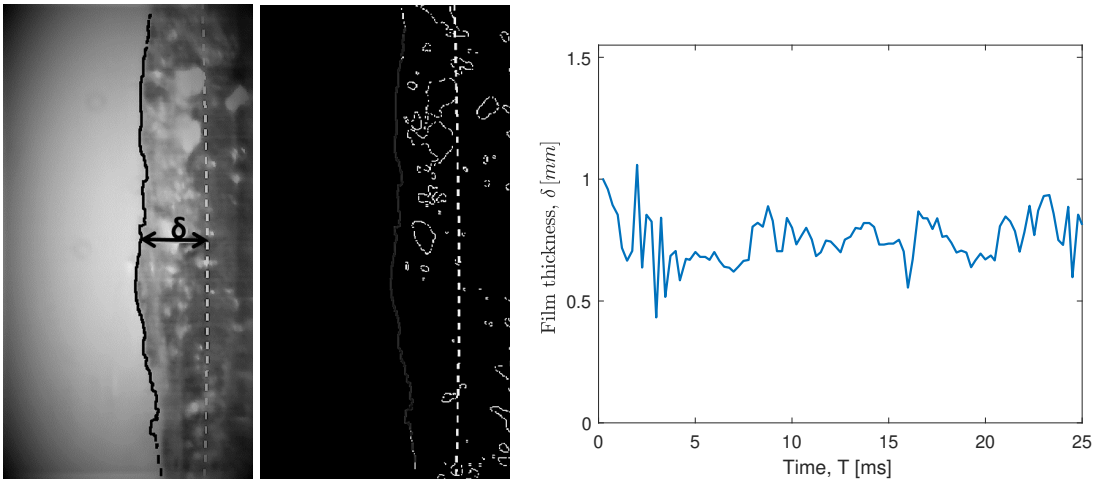

(a) (b) (c)

Fig. 3: (a) Instantaneous filtered image (δ) identified for this image (b) processed image for edge detection (c) An example of instantaneous film thickness (δ) against time for 100 individual processed images at P2.

The oil film thickness profile in the present study is unsteady and non-uniform (example shown in Fig. 3a), and at some operational conditions it is covered with waves and small ripples. It was necessary to develop an automated technique to measure transient variation in film thickness. The continuous and dashed lines in Fig. 3a and 3b represent the film interface and the wall, respectively. The distance between them is the instantaneous film thickness (δ). In the present study, these lines were identified using image processing in MATLAB R2020a and a brief description of the procedure is given below.

Each image is loaded and sharpened using MATLAB as shown in Fig. 3a. The image is then binarized to produce a black and white image which is determined by the grayscale value of each pixel. The area of the image where droplets and darker areas of the image occur is then masked off by setting all of the pixels past a specific column to white. This prevents these elements from affecting edge detection. Canny edge detection is applied to the image, finding the locations of all the pixels where a colour change occurs and this is used to identify the edge of the oil layer. An image showing the result of the edge detection is shown Fig. 3b. The position of the rows within P2/P4 that are exactly at the $90°/270°$ positions is known from the wall coordinates. Therefore, δ identified in Fig. 3a in pixels between the wall coordinate and the edge of the oil film can be found at this exact location. This distance δ identified in Fig. 3a is multiplied by the calibration factor to give the thickness value in mm. This approach gives the film thickness value (δ) for every image.

An example of the variation with time of the obtained instantaneous film thickness data for 100 individual processed images is shown in Fig.3c for P2.

The presence of droplets and ligaments can change the pixel intensity of the images, thus affecting the film thickness data by producing obvious outlier values. Hence, in the present study, outliers were removed and the instantaneous film thickness data is smoothed to remove any background noise (fluctuations) due to droplets/ligaments. These outliers could be detrimental as they could be amplified during further analysis and also they could influence the statistical values. Further analysis of the wave statistics was carried out of the film thickness values to give a better understanding of the characteristics of the waves in such a complex flow.

CHARACTERIZATION OF THE FLOW BASED ON FILM INTERFACE

As a first step, a qualitative investigation was carried out to identify distinct regimes, which will give a better understanding of the effect of gravity and shear on the film interface at the different conditions. Instantaneous images for various Re_ω at $Re_{Liq.} = 9$ and L_L for P2 and P4 locations are exhibited in Fig. 4. Figure 4a, for clarity, illustrates the region of interest representing the film interface (labeled "Air-oil interface") along with the direction of forces. The difference in the film interface shape at P2 and P4 is due to the coupled effect of gravity and shear which are relevant for the images in Fig. 4b. The gravity forces have more influence at P2 as compared to P4 at low Re_ω since the rotational airflow and gravity are in the same direction at P2 (co-current flow). In contrast, the gravity and shear forces act in the opposite directions at P4 and the gravity effect was found to be dominant at P4 only for $Re_\omega \leq 0.57 \times 10^6$, above which the interfacial shear starts to become the dominate force affecting the flow field. The increasing interfacial shear causes the droplets and ligaments to flow upward above this value of Re_ω.

It is possible to categorise the shape of the oil-film interface based on the wave sizes and the various shapes are exhibited in Fig. 5a. These shapes are also seen in the results by Hee et al. [13] in their study investigating the flow uniformity in the co- and counter current region. In this study, the film interface is categorized into three different shapes - longwave (LW, long wavelength), shortwave (SW, short wavelength), and uniform film (UF, no waves). In the present study, LW and SW were differentiated based on the ratio of wave-length to wave-height. If the ratio between them is $\geq$ 10, then it is categorized as long wave, else it is categorized as short wave. As the name suggests, the uniform film indicates that the oil-film thickness along the bearing is uniform without the presence of any distinguishable wave features due to high interfacial shear. This is observed at $Re_\omega \geq 1.28 \times 10^6$. The probability of ligament and droplet shedding

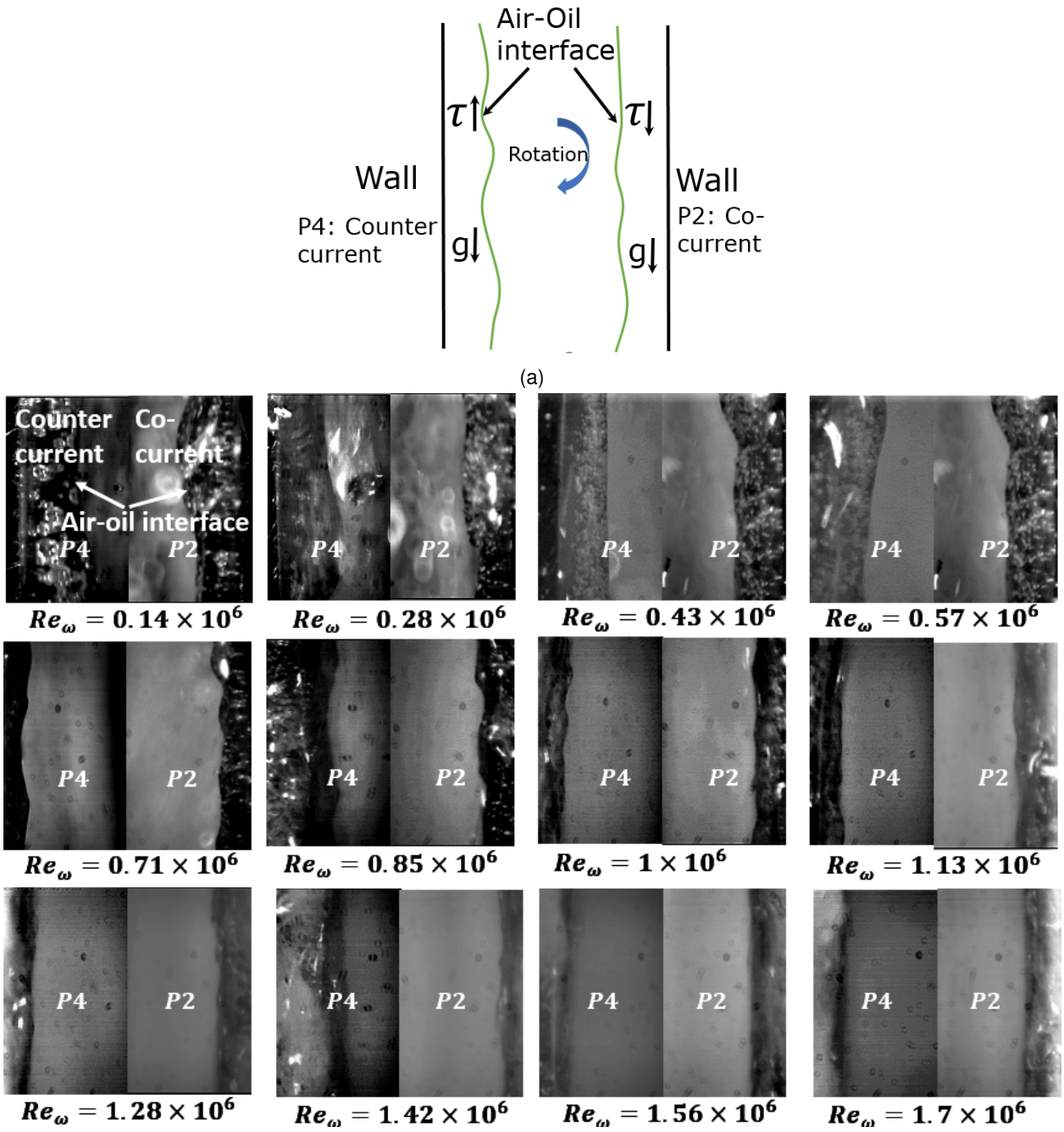

Fig. 4: (a) Direction of the governing forces at P2 and P4. τ and g represent the interfacial shear stress and gravity, respectively. The arrow marks the direction of the forces. The air-oil interface is the region of interest. (b) instantaneous images for various Re_ω at $Re_{Liq.} = 9$ and L_L. P4 and P2 represent the counter-current and co-current locations respectively.

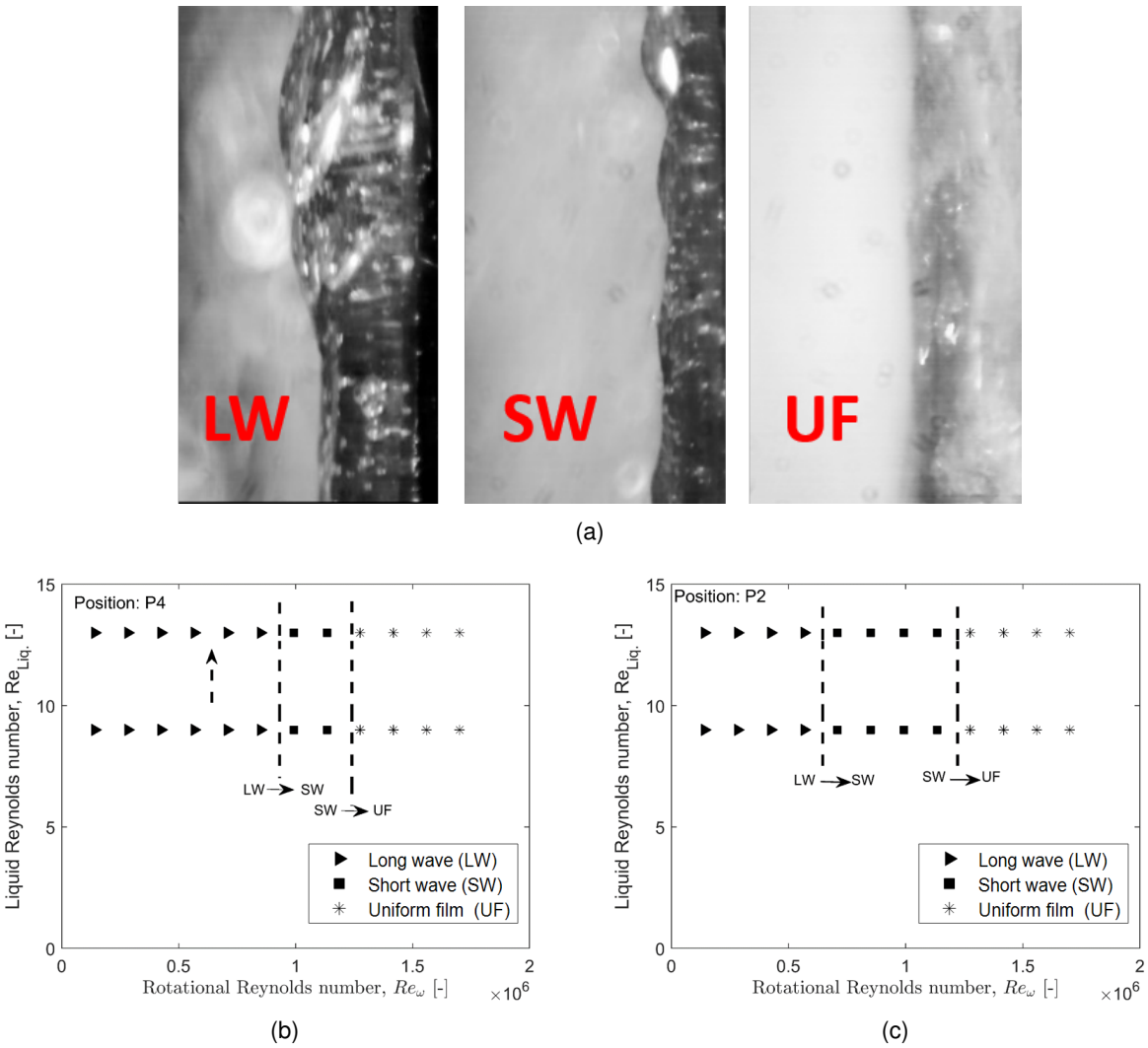

Fig. 5: (a) Examples of different shapes of the film interface: Long wave (LW), Short wave (SW), and Uniform film (UF). Regime map based on the shape of the film interface for (b) P4 (c) P2 . The arrow indicates the change in the flow direction at P4. The dashed lines represent the probability of the change in the interface at that Re_ω.

from the oil film when it interacts with rotational air will be higher for shorter wave-length as compared to longer wave-length. These ligaments and droplets will impinge on the oil film resulting in the formation of bubbles [15], and consequently, will affect the heat transfer phenomenon of the oil.

Two interesting observations can be made from Fig. 4b as Re_ω increases. It is known that the interfacial shear increases as Re_ω increases [16] as it corresponds to increased gas speed. Firstly, the quantity of droplet/ligaments formed was found to increase as Re_ω increases and secondly, this increase in interfacial shear causes the film interface to change from a long wave at 0.14×10^6 to a uniform film at 1.28×10^6. It

was observed that at higher Re_ω ($Re_\omega \geq 1.28 \times 10^6$), the behaviour of both sides is found to be the same. This suggests that in considering the ratio of shear to gravity forces there is a critical value or range above which the effect of gravity is negligible.

A regime map based on the above film interface shapes at various Re_ω is shown in Fig. 5. It is observed from Fig. 5b and 5c that the shape of the film interface changes from longwave (LW) to shortwave (SW) around $Re_\omega = 0.85 \times 10^6$ for P4 and around $Re_\omega = 0.57 \times 10^6$ for P2. This indicates that the film interface has more waves at the P4 side for a higher range of Re_ω as compared to the P2 side (more uniform). This interesting observation can be explained by considering the fact the interfacial shear and gravity are acting in the opposite direction at P4. Consequently, this will reduce the net force on the oil film on the P4 side as compared to the P2 side. This relative reduction in the net force generates waves more easily at the P4 location as compared to the P2 location. This undulation causes the film to move in a non-uniform wavy manner. The change in the flow direction at P4 due to higher interfacial shear as compared to gravity forces is marked by the dotted arrow in Fig. 5b. With a further increase in Re_ω, the film interface for both positions changes from SW to UF, indicating the rotational shear is dominating the film interface shape.

CHARACTERIZATION OF THE FLOW BASED ON OIL FILM-THICKNESS

The variation of the non-dimensional median oil film thicknesses (δ_{median}) obtained at the co-current (P2) and counter-current region (P4) is plotted in Fig. 6a. The median is chosen instead of the mean because statistically the median is considered more representative for skewed distributions. If the distribution is symmetric (zero skewness), then the magnitude of the median and the mean will be the same, which is why it is usual to use the mean for normal distributions, which are symmetric. In the present study, the distribution of the film thickness is not a normal distribution, which can be verified by looking at distribution plot shown later in Fig. 8. The median film thickness is non-dimensionalized with the hydraulic diameter (D_h= $\frac{2X(r_c-r_s)}{X+r_c-r_s}$). Here X and r_c represent the axial length and outer radius of the bearing slot; r_s is the shaft radius.

As expected from other multi-phase flow applications [6, 15] it is observed from Fig. 6a, that with an increase in Re_ω the film thickness at both P2 and P4 reduces. This decrease in film thickness with Re_ω is because an increase in the Re_ω leads to an increase in the speed of the rotational airflow which increases the interfacial shear between the oil and air. Consequently, this will result in a higher film velocity, and through the continuity equation, causes a lower film thickness for the same volume of liquid throughput. It should be noted that in gas-sheared flows, droplets and ligaments are sheared off from the liquid surface

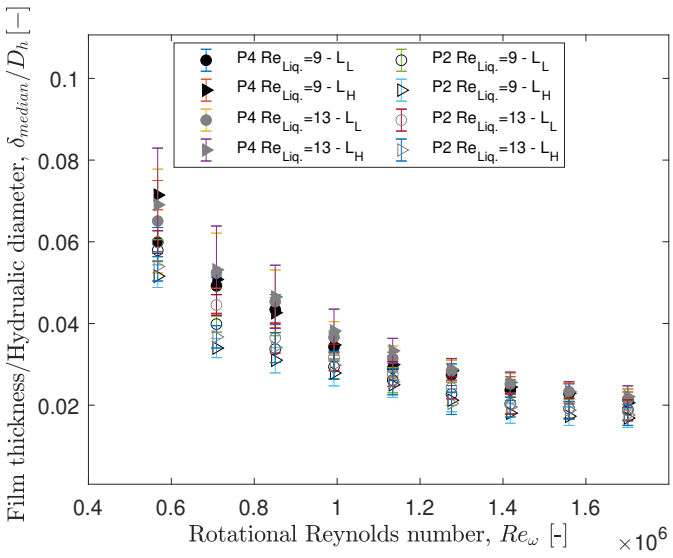

(a)

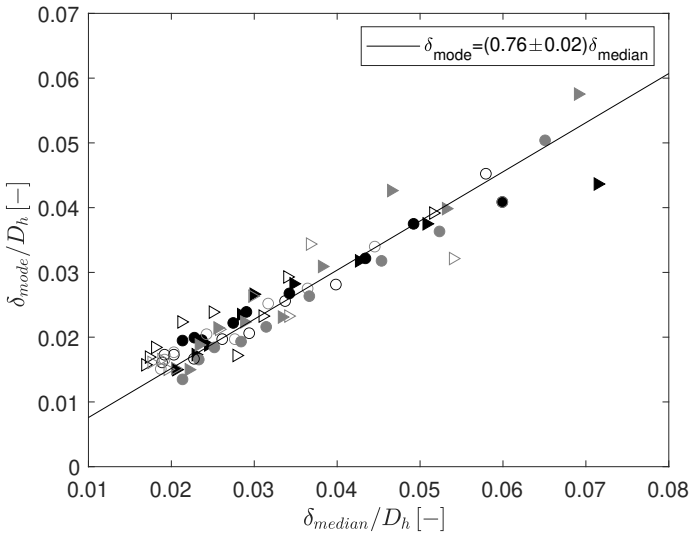

(b)

Fig. 6: (a)Non-dimensional median film thickness against various Re_ω, $Re_{Liq.}$ and loads at the co-current (P2) and counter current region (P4) (b) relationship between the film thickness obtained using median and the mode.

due to interfacial shear and the entrainment of droplets and ligaments in the gas-core increases with the increase in gas velocity [17, 18]. Thus, in the present study, the tearing off droplet/ligaments from the liquid surface would also result in the decrease in the film thickness. The independent effect of film Weber number, calculated based on film height, oil properties and gas velocity, has not been evaluated in this study because a single oil with a single supply temperature has been used. It can be theorised that decreased surface

tension (higher film Weber number) would lead to an increase in the number of ligaments but reduce the film speed.

From Fig. 6a, two interesting observations can be made. Firstly, for $Re_\omega \leq 1.13 \times 10^6$, the δ_{median}/D_h at the P2 location is lower than the P4 location for any particular oil flow rate and load, which is because at the P2 region the flow is co-current. Therefore, the forces act in the same direction which more strongly accelerate the film leading to a reduction in the film thickness magnitude. As expected, with the increase in $Re_{Liq.}$, an increase in the film thickness value was observed at a particular Re_ω and load. Interestingly, the effect of load on δ_{median}/D_h behaves differently in the P2 and P4 locations. While δ_{median}/D_h increases with load at P4, it decreases with an increase in load at P2. From the oil flow meter placed at the front and the rear outlets, it was confirmed that the oil flow rate does not change significantly ($< 5\%$) with the increase in load for various Re_ω. A potential answer for this conundrum could be figured out by measuring the interfacial shear, which is out of scope in the present study. Secondly, it was observed in Fig. 6a that from Re_ω = 1.28×10^6, which is in the uniform film regime, the film asymptotically reaches a constant value. This indicates that the film is accelerated to its fastest limit as noted in other multi-phase applications [19].

The relationship between the mode and the median values of the film thickness is shown in Fig. 6b. The modal value (obtained directly from MATLAB and representing the most commonly occurring film thickness value) in the present study could also be considered as representative of the thickness of the base film. Moreover, the presence of small amplitude ripple waves on the base film reduces the variation in the base film thickness, hence, it can be represented by the modal value of the film thickness record.

The solid black line represents a best fit equation in Fig. 6b by considering all the values of film thickness at various flow rates, loads and Re_ω. The power fit equation is shown in Fig.6b, with 95% error bounds on the constant. From Fig. 6b it was observed that most of the off line values are concentrated between 0.02 and 0.04, which shows the base film thickness is limited to a specific range of thickness and the increase in the modal magnitude is due to the effect of oil flow rate, interfacial shear and gravity.

In two-phase pipe flow applications [11, 20], relationships have been developed between the interfacial friction factor and the liquid and gas Weber numbers, on the basis that film thickness is a function of interfacial friction factor. Extending from that, in Fig. 7 normalised median film thickness is plotted against a non-dimensional function of gas and liquid Reynolds numbers ($Re_\omega/Re_{Liq}^{0.25}$). The filled symbols represent the four data sets at P4 (low and high loads, lower and higher flowrates) and it is suggested that these data points can be represented by two curves with transition occurring at $Re_\omega = 0.93 \times 10^6$. The change in the curve from steeper to shallower corresponds to the change in the flow regime from long wave to short wave.

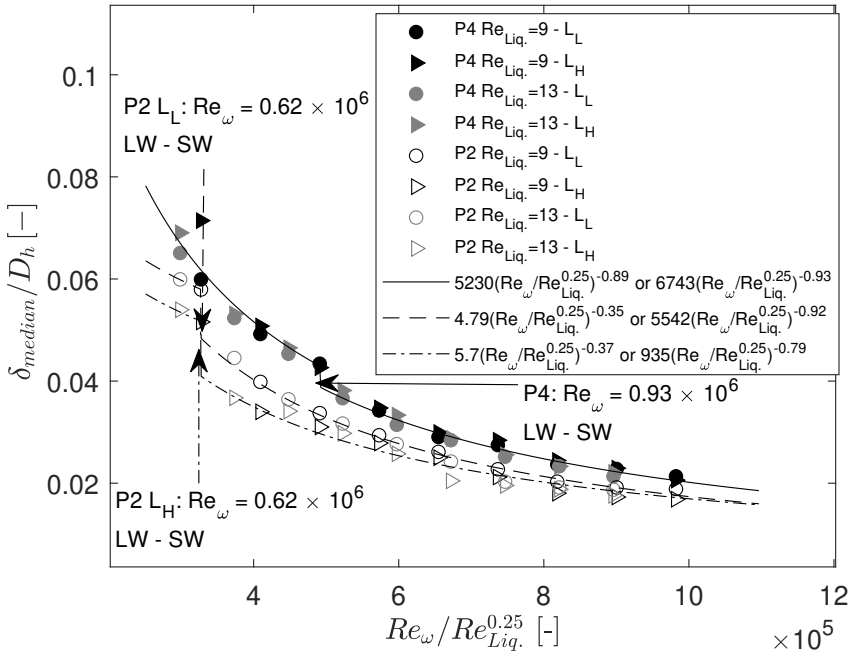

Fig. 7: Relationship between normalized median film thickness against $Re_\omega/Re_{Liq.}^{0.25}$. The arrow indicates the change in the slope of the curve.

The open symbols represent the corresponding four data sets for P2. Here it is observed that there are different relationships for each load, and as with P4, curves can be fitted to the data for low and high Re_ω. Interestingly, it is observed from Fig. 7 that the change in slope of the P2 curves for both the loads occurs at Re_ω = 0.62×10^6. This change in the slope for P2 corresponds to the change in the film interface from long-wave to short-wave as shown in the regime map in Fig. 5c.

The above result indicates that though the present relationship linking film thickness and surface behaviour to shaft speed (Re_ω) and oil flow rate works well for various oil flow rates, further investigation is required to fully understand the effects of gravity vs. air shear and load. It is known that the heat generated in a bearing increases with load as well as shaft speed. Although calculating Re_{Liq} based on local oil temperature may have some benefit, this would not wholly account for the difference between the P2 and P4 data sets since the effect of load is greater at P2 compared to P4.

The probability distribution function of the film thickness for a few different cases is shown in Fig. 8. The purpose of Fig. 8 is not only to show that the film thickness distribution is not normal but also how the thickness distribution changes under different conditions. With the increase in Re_ω from Re_ω = 0.71×10^6 to 1.13×10^6, the normalized median film thickness reduces as shown in Fig. 8a. Qualitatively, it is also

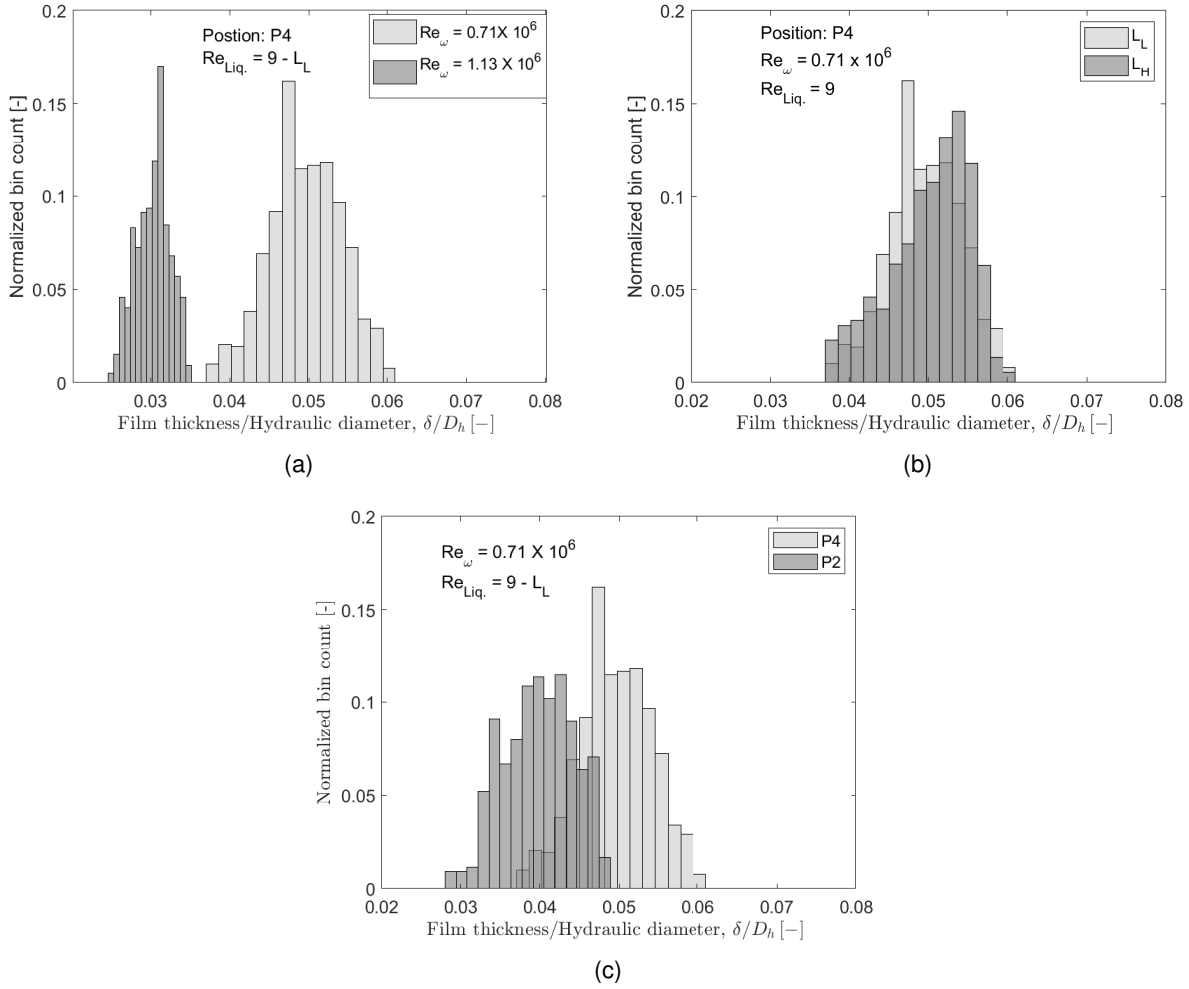

Fig. 8: Probability distribution function of the film thickness comparing (a) two different Re_ω (1.13×10^6 and 1.7×10^7) at P4 for a particular load and $Re_{Liq.}$ (b) two different loads (L_L and L_H) at P4 for a particular Re_ω and $Re_{Liq.}$ (c) P4 and P2 for a particular load, Re_ω and $Re_{Liq.}$

observed from Fig. 8a that the distribution for the lower Re_ω is narrower as compared to the higher Re_ω, which indicates that the film surface is more uniform at higher Re_ω. This uniformity in the film thickness is because of the increase in interfacial shear and centrifugal force. With the increase in load from L_L to L_H, it was observed from Fig. 8b, that the film thickness distribution does not change significantly: it shifts slightly towards the right indicating higher thickness. This small shift in the film thickness distribution indicates that the shaft speed has more impact as compared to load. An increase in film thickness implies that the film is moving more slowly due to continuity. The coupling effect of gravity and interfacial shear is noticeable in Fig. 8c. The effect of forces in the same direction causes the film thickness at P2 to be lower than at P4

where they oppose. It can be inferred that the film at P2 moves faster than the film at P4.

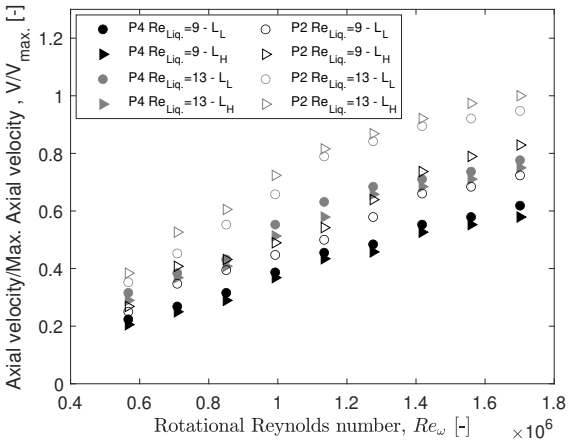

Fig. 9: Normalized bulk axial velocity against various Re_ω, $Re_{Liq.}$ and loads at the co-current (P2) and counter current region (P4).

The bulk axial velocity of the fluid was estimated using the oil film thickness measurements and the rig-front exit oil mass flow rate as shown in eqn. 1. The front exit mass oil flow rate was obtained based on the mass conservation between the front exit and the outlet.

$$V = \frac{Q_{front}}{\rho_{front}\pi(r_c^2 - (r_c - \delta)^2)} \tag{1}$$

The other parameters in eqn.1 are known from other measurements. The bulk axial velocity is normalized with the maximum bulk velocity (V_{max}). It is observed from Fig.9 that the bulk axial velocity increases with an increase in Re_ω. This increase in the bulk axial velocity is expected as the higher interfacial shear will transfer more momentum from the gas to the liquid as Re_ω increases. The front exit oil flow rate Q_{front} increases by $\approx$ 20% as the liquid flow rate goes from $Re_{Liq.} = 9$ to $Re_{Liq.} = 13$. This directly causes an increase in V/V_{max} due to the higher oil flow rate. V/V_{max} is higher at P2 as compared to P4 as the gravity and interfacial shear assist in accelerating the film. As expected, the effect of film thickness on V/V_{max} was found to be inversely proportional to the film thickness. This is to maintain continuity balance. It is also observed from Fig.9 that V/V_{max} does not change significantly at higher Re_ω ($Re_\omega \geq 1.28 \times 10^6$). This means the magnitude of film thickness reaches a plateau and the film is stabilising at a higher Re_ω.

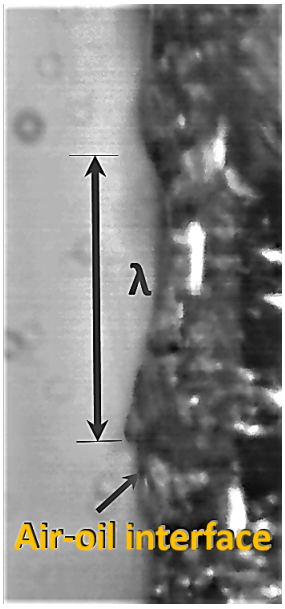

Fig. 10: Schematic diagram of the determination of the wave-length from the images.

Wave characteristics

The new image processing technique mentioned above produces time-varying thickness measurements which allows for a greater range of analysis methods such as the measurement of wave characteristics. The wavelength of surface waves for a particular flow condition is obtained by determining the distance between two successive crests of the wave as shown in Fig. 10. The wave-length is normalized with the hydraulic diameter.

For investigating wave characteristics, Re_ω values up to 1.13×10^6 were considered. This is because above Re_ω = 1.13×10^6, the film is mostly uniform without the presence of any discernible waves. From Fig. 11a, it is observed that the normalized wavelengths show a linearly decreasing relationship with Re_ω, with values ranging from 0.33 – 0.41 at Re_ω = 0.57×10^6, for all conditions, decreasing to a range of 0.17 – 0.21 at Re_ω = 1.13×10^6. No significant effect of location, load and $Re_{Liq.}$ on the wavelength was observed. Although no significant effect of load was anticipated, it is somewhat surprising to see no effect of $Re_{Liq.}$. As expected, a decrease in the wavelength leads to an increase in the frequency of the waves as shown in Fig. 11b. Similar to the measurement of wavelength, the effect of load and flow rate was not observed in the frequency calculation.

In the present study, the critical wavelength that defines whether or not waves are gravity waves, $\lambda_C = 2\pi\sqrt{(\frac{\sigma}{g(\rho_{Liq.}-\rho_{gas})})}$, was found to be 11.8 mm. The values for surface tension and densities were obtained from measurements made on the oil used in the rig. In the present study, $\frac{\lambda}{\lambda_C}$ is less than unity for all cases

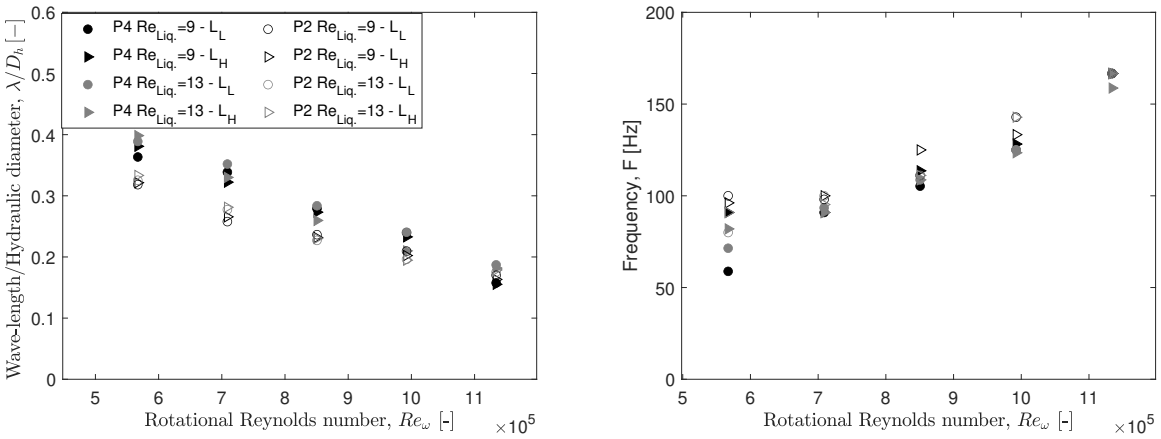

(a) (b)

Fig. 11: Shows the (a) normalized wave-length against Re_ω (b) Frequency of the waves

(the maximum value of $\frac{\lambda}{\lambda_C}$ is close to but below 1), demonstrating that the wavelengths are less than the critical value. This indicates that capillary waves are the ones present in the oil layer and surface tension forces are the dominating effect, as opposed to gravity-capillary waves which occur when fluid inertia has a more prevalent influence.

DISCUSSIONS ON THE EFFECT OF GRAVITY AND INTERFACIAL SHEAR ON HEAT TRANSFER

The work here has shown that with the increase in Re_ω, the film thickness decreases asymptotically towards a constant value at high Re_ω. Therefore, the gravity effect on the heat transfer process will be negligible at high Re_ω. Thus, the discussion regarding the heat transfer characteristics inside bearing chamber in this section is based on the scenarios where the flow is dominated by interfacial shear. At high Re_ω, a strong shear can lead to a super-critical flow where droplets will be shed from the film impinging at a different location. These impinging droplets on the liquid film are found to be a primary source of bubble generation in gas-sheared flows [17, 18]. It is conjectured that if a significant number of bubbles gets entrapped in the liquid film, it will be detrimental for the scavenge pump and may also degrade the cooling process inside the bearing chamber by acting as an insulator between the wall and the film surface. Qualitatively, it was observed from the present study that the number of droplets and ligaments formed increases with an increase in Re_ω. Further studies will need to look at developing an improved understanding of the droplet and bubble spectra at higher rotational Re_ω.

It is further observed from the images and film statistics that the relative values of the interfacial shear

and gravity forces have an effect on the film thickness that varies with location. It has already been observed that at P2 the film is thinner compared to P4 because the gravity and the shear are acting in the same direction. The heat transferred from the walls to the film at P2 will be carried by the film directly towards the scavenge whereas the heat transferred to the film at P4 will be carried around the chamber before reaching the scavenge. At P2 gravity accelerates the film thereby enhancing heat transfer whereas at P4 the film moves slower, but the film will be cooler there than at P2. The heat transfer situation is clearly complex and highly interactive, and therefore, merits further investigation if more efficient engines with reduced impact on the environment are to be designed in the future.

CONCLUSION

This work is focused on understanding the effect of interfacial shear and gravity on the film characteristics in an aero-engine bearing chamber. This understanding could potentially lead to more efficient oil-flow systems which could allow engineers to build more environmentally friendly aero-engines. In this paper the oil flow characteristics at the co- and counter current locations were investigated using high speed imaging equipment. Images were collected and analysed to investigate the oil film characteristics at a range of aero-engine relevant operating conditions by varying the Re_ω, oil flow rate, and axial loading on the bearing.

From the investigation, three main conclusions are obtained. The first is that from qualitative observation of the instantaneous images three film interface regimes exist: long wave, short wave and uniform film. The critical shaft Re_ω for long wave to short wave transition was not the same at P2 and P4. It can be concluded that both the interfacial shear and gravity influence the film interface at low $Re_\omega < 0.57 \times 10^6$. At $Re_\omega > 1 \times 10^6$, the flow transitions from short wave to uniform film. It is believed that this is because the interfacial shear starts to dominate the flow. Moreover, from the regime map, it can be concluded that for low $Re_\omega < 0.57 \times 10^6$, the effect of gravity and interfacial shear at P4 is to stabilize the flow as they are acting in the opposite direction.

From the film statistics, this paper shows that the film thickness decreases with increase in Re_ω. Above Re_ω = 1.13×10^6, the film thickness does not change significantly. It is believed this is due to the effect of shear. Jumps in the film thickness are noted when the wave regime changes with thicker films associated with long waves and the thinnest film is associated with uniform film.

With regard to wavelength, it was shown that for all conditions investigated the wavelengths are smaller than the critical value of 11.8 mm demonstrating that the waves are capillary waves not gravity waves. This means that surface tension forces (which are dependent on temperature) are the dominant effect.

Overall this work has made a significant contribution to knowledge while at the same time highlighting that this a very complicated situation and that further work needs to be done to understand the complex fluid flow and heat transfer processes to support future, more efficient, aero-engine design.

ACKNOWLEDGEMENTS

This project has received funding from the Clean Sky 2 Joint Undertaking under the European Union's Horizon 2020 research and innovation programme under grant agreement No 724625. The authors are grateful for the technical and financial support provided by Rolls-Royce.

REFERENCES

[1] Glahn, A., Busam, S., Blair, M., Allard, K., and Wittig, S., 2002. "Droplet generation by disintegration of oil films at the rim of a rotating disk". *J. Eng. Gas Turbines Power,* **124**(1), pp. 117–124.

[2] Willenborg, K., Busam, S., Roßkamp, H., and Wittig, S., 2002. "Experimental studies of the boundary conditions leading to oil fire in the bearing chamber and in the secondary air system of aeroengines". In Turbo Expo: Power for Land, Sea, and Air, Vol. 36088, pp. 739–747.

[3] Santhosh, R., Hee, J. L., Simmons, K., Johnson, G., Hann, D., and Walsh, M., 2017. "Experimental investigation of oil shedding from an aero-engine ball bearing at moderate speeds". In ASME Turbo Expo 2017: Turbomachinery Technical Conference and Exposition, American Society of Mechanical Engineers Digital Collection.

[4] Aidarinis, J., Missirlis, D., Yakinthos, K., and Goulas, A., 2011. "Cfd modeling and lda measurements for the air-flow in an aero engine front bearing chamber". *Journal of engineering for gas turbines and power,* **133**(8).

[5] Peduto, D., 2015. *Oil Droplet Impact Dynamics in Aero-Engine Bearing Chambers-Correlations derived from Direct Numerical Simulations*. Logos Verlag Berlin GmbH.

[6] Wittig, S., Glahn, A., and Himmelsbach, J., 1993. "Influence of high rotational speeds on heat transfer and oil film thickness in aero engine bearing chambers". In Turbo Expo: Power for Land, Sea, and Air, Vol. 78903, American Society of Mechanical Engineers, p. V03AT15A060.

[7] Glahn, A., and Wittig, S., 1995. "Two-phase air/oil flow in aero engine bearing chambers: Characterization of oil film flows". In Turbo Expo: Power for Land, Sea, and Air, Vol. 78781, American Society of Mechanical Engineers, p. V001T01A026.

[8] Guoding, C., Hengchao, S., and Jun, W., 2011. "Research into configuration and flow of wall oil film in

bearing chamber based on droplet size distribution". *Chinese Journal of Aeronautics,* **24**(3), pp. 355–362.

[9] Gorse, P., and Busam, S. D., 2006. "Influence of operating condition and geometry on the oil film thickness in aero-engine bearing chambers". *Journal of Engineering for Gas Turbines and Power,* **128**, pp. 103–110.

[10] Kurz, W., Dullenkopf, K., and Bauer, H.-J., 2013. "Capacitive film thickness measurements in a ventless aero-engine bearing chamber—influence of operating conditions and offtake design". *Journal of engineering for gas turbines and power,* **135**(11).

[11] Ju, P., Liu, Y., Brooks, C. S., and Ishii, M., 2019. "Prediction of interfacial shear stress of vertical upward adiabatic annular flow in pipes". *International Journal of Heat and Mass Transfer,* **133**, pp. 500–509.

[12] Chandra, B., Simmons, K., Pickering, S., Collicott, S. H., and Wiedemann, N., 2013. "Study of gas/liquid behavior within an aeroengine bearing chamber". *Journal of engineering for gas turbines and power,* **135**(5).

[13] Hee, J. L., Santhosh, R., Simmons, K., Johnson, G., Hann, D., and Walsh, M., 2017. "Oil film thickness measurements on surfaces close to an aero-engine ball bearing using optical techniques". In Turbo Expo: Power for Land, Sea, and Air, Vol. 50923, American Society of Mechanical Engineers, p. V07AT34A017.

[14] Hee, J. L. "Experimental and computational investigation into oil shedding from an aeroengine ball bearing". PhD thesis, University of Nottingham.

[15] Sinha, A., Cherdantsev, A., Johnson, K., Vasques, J., and Hann, D., 2021. "How do the liquid properties affect the entrapment of bubbles in gas sheared liquid flows?". *International Journal of Heat and Fluid Flow,* **92**, p. 108878.

[16] Kakimpa, B., Morvan, H., and Hibberd, S., 2017. "A coupled 1d film hydrodynamics and core gas flow model for air-oil flows in aero-engine bearing chambers". In Turbo Expo: Power for Land, Sea, and Air, Vol. 50794, American Society of Mechanical Engineers, p. V02BT41A045.

[17] Hann, D. B., Cherdantsev, A. V., and Azzopardi, B. J., 2018. "Study of bubbles entrapped into a gas-sheared liquid film". *International Journal of Multiphase Flow,* **108**, pp. 181–201.

[18] Cherdantsev, A. V., Sinha, A., and Hann, D. B., 2022. "Studying the impacts of droplets depositing from the gas core onto a gas-sheared liquid film with stereoscopic bblif technique.". *International Journal of Multiphase Flow*, p. 104033.

[19] Cherdantsev, A. V., Hann, D. B., and Azzopardi, B. J., 2014. "Study of gas-sheared liquid film in

horizontal rectangular duct using high-speed lif technique: Three-dimensional wavy structure and its relation to liquid entrainment". *International Journal of Multiphase Flow,* **67**, pp. 52–64.

[20] Sawant, P., Ishii, M., Hazuku, T., Takamasa, T., and Mori, M., 2008. "Properties of disturbance waves in vertical annular two-phase flow". *Nuclear Engineering and Design,* **238**(12), pp. 3528–3541.